Bull. Mater. Sci. (2018) 41:113
https://doi.org/10.1007/s12034-018-1629-8

Sn^{4+}-doped TiO_2 nanorod array film with enhanced visible light photocatalytic activity

SHINING NI, TIANTIAN ZHOU, YUANNA ZHU, YONGQIANG CAO* and PING YANG
School of Material Science and Engineering, University of Jinan, Jinan 250022, People's Republic of China
*Author for correspondence (mse_caoyq@ujn.edu.cn)

MS received 22 August 2017; accepted 26 December 2017; published online 30 July 2018

Abstract. Sn^{4+}-doped TiO_2 nanorod array film (NAF) on the fluorine-doped tin oxide (FTO) conducting glass was successfully synthesized using the facile hydrothermal method. The NAF photocatalysts were characterized by the scanning electron microscopy (SEM), X-ray diffraction (XRD) and UV–Vis diffuse reflectance spectra (DRS). The SEM images showed that both doped and pure TiO_2 NAFs exhibited a good nanorod array structure. Sn^{4+}-doped TiO_2 NAF still maintains rutile crystal structure, which was identical to that of pure TiO_2 sample. By means of the DRS measurement, it was found that the Sn^{4+} doping in TiO_2 nanorod could induce an obvious enhancement of visible light absorption owing to the introduction of doping energy level in the band gap of TiO_2. The degradation of methyl orange (MO) demonstrated that the Sn^{4+}-doped TiO_2 NAF exhibited an enhanced photocatalytic activity than pure TiO_2 NAF under the visible light ($\lambda > 400$ nm) irradiation, which should be attributed to the enhanced visible light response and improved separation efficiency of photogenerated carriers of Sn^{4+}-doped TiO_2.

Keywords. TiO_2 film; nanorod array; Sn^{4+}; ion doping; photocatalyst.

1. Introduction

Over the last two decades, semiconductor-based photocatalysts have attracted increasing attention due to their potential applications in the degradation of environmental contaminants and conversion of solar energy [1–5]. With the deep research in photocatalysis, many semiconductor-based photocatalysts, such as TiO_2 [6,7], ZnO [8], WO_3 [9], BiOCl [10], BiOBr [11], BiOI [12], C_3N_4 [13], Ag_3PO_4 [14], etc. were found and investigated systematically by the material scholars. Among the aforementioned many photocatalysts, due to the high photocatalytic activity, high physical and chemical stability, nontoxicity and cheap price, TiO_2 was believed to be one of the most potential photocatalyst of all the time, and it payed significantly more attention by the researchers [15]. However, the wide band gap of TiO_2 (3.0–3.2 eV) caused that it can only absorb the ultraviolet of sunlight (there is only 5% in the sunlight), so, the TiO_2 exhibits a relative lower visible photocatalytic activity. In addition, the quick recombination of photogenerated electron–hole pairs in TiO_2 could also further reduce the photocatalytic activity verified by the relevant researchers [16–18].

To enhance the visible light response of TiO_2, the ion doping method was proposed and carried out in many research works. Zhou *et al* [19] prepared the self-organized polycrystalline F-doped TiO_2 hollow microspheres, and the flower-like F-doped TiO_2 hollow microspheres showed the high photocatalytic activity for the degradation of methylene blue (MB) under visible-light irradiation. Using a green approach, doped-TiO_2 single crystals with metal, nonmetal and rare earth elements was synthesized by Long *et al* [20], and all the doped photocatalysts showed the much higher visible activity compared to the undoped TiO_2. Shao *et al* [21] also investigated the electronic properties of rutile TiO_2 with nonmetal dopants (N doping, C doping, N+H codoping and C+H codoping) using the first-principle density functional theory. Lots of research results implied that both the metal and nonmetal ions doped in TiO_2 can generate the doping energy levels in the band gap of TiO_2. These doping energy levels could lead to the enhanced visible light absorption and separation efficiency of photogenerated electron–hole pairs, and subsequently, to the improvement of visible activity of TiO_2.

Because the photocatalytic reaction is an interfacial reaction taking place at the surface of photocatalyst, the specific surface area of photocatalyst is another key factor influencing the photocatalytic activity. Though the film-type photocatalysts have a greater potential application in the removal of pollutants from water, attributing to its well recoverability, lower specific surface area of flat film than nanopowder would lead to the decrease of its photocatalytic activity. TiO_2 nanorod array film (NAF) has an ultra high specific surface area comparing with conventional flat film owing to its unique nanorod array structure, and a much higher photocatalytical activity is also observed correspondingly. Fu *et al* [22] constructed a new composite photocatalyst of CdSe-sensitized TiO_2 nanorod array grown on fluorine-doped tin oxide (FTO) coated with a TiO_2:Yb^{3+}, Er^{3+} thin film. Due to the large specific surface area of nanorod array

structure, extended absorption of TiO_2 and the reduction of electron–hole recombination, the composite film exhibited the improved photocatalytic efficiency. Flower-like branched TiO_2 nanorod arrays with the surface anatase/rutile junctions on FTO were successfully fabricated by a modified hydrothermal method by Liu *et al* [23], and the film showed excellent photocatalytic properties by means of photoelectrochemical (PEC) measurements.

Generally, the TiO_2 NAFs synthesized with hydrothermal method were rutile crystal structure (band gap $\sim$ 3.0 eV). The prepared rutile TiO_2 nanorod arrays have a high UV photocatalytic activity because of their rod-array structures, but usually, a much weaker activity under visible-light irradiation is observed due to its weak visible light response. Here, to improve the visible light response of rutile TiO_2 NAFs, we have successfully prepared the Sn^{4+}-doped TiO_2 NAFs by the facile hydrothermal method. Owing to the Sn^{4+} ion-doping, the NAFs showed a positive enhancement to visible absorption. The enhanced visible absorption and improved separation efficiency of photogenerated carriers due to the introduction of Sn^{4+} doping energy level synergistically lead to the high visible activity of Sn^{4+}-doped TiO_2 NAFs.

2. Experimental

2.1 *Materials*

Tetrabutyl titanate, hydrochloric acid (12 M) and $SnCl_4$ were all analytical grade and purchased from Shanghai Guoyao Chemical Industry Co. Ltd. The other chemicals were used without further purification. Ultrapure water ($>18\ M\Omega \cdot cm$) was used for all the experiments.

2.2 *Preparation of NAFs*

All the NAFs were prepared via a simple hydrothermal method. For the preparation of Sn^{4+}-doped TiO_2 NAF, 30 ml of ultrapure water and 30 ml of hydrochloric acid (12 M) were mixed and stirred for 15 min. One millilitre of tetrabutyl titanate was added to the above mixture and stirred for 20 min. Different volumes of $SnCl_4$ (340, 510 and 850 µl denoted as TiO_2–340Sn, TiO_2–510Sn and TiO_2–850Sn) were respectively, added to the above mixture under the magnetic stirring for another 20 min. The as-prepared solution was transferred to a 100 ml autoclave with a Teflon liner, and the FTO conducting glass (5.7 × 2.5 cm) was immersed into the autoclave, which was heated at 150°C for 12 h, and then naturally cooled to ambient temperature. The resulting film was washed with distilled water and absolute alcohol for several times to remove residual ions. The final products were then dried at 70°C for 2 h prior to characterization. The pure TiO_2 NAF (denoted as TiO_2) was prepared using the similar procedures as above, but without adding $SnCl_4$.

2.3 *Characterizations*

The UV–Vis diffuse reflectance spectra (DRS) were collected on a UV–Vis spectrometer (UV-4100, Hitachi). $BaSO_4$ was used as the reflectance standard in the experiment. The morphology of films was observed using a field emission scanning electron microscope (FESEM) (QUANTA FEG 250, FEI). The energy-dispersive X-ray spectroscopy (EDS) of Sn^{4+}-doped TiO_2 NAFs were acquired with EDS spectrometer fitted on the microscopy. The X-ray diffraction (XRD) patterns of the film samples were measured on an X-ray diffractometer (D8 ADVANCE, Bruker) with a CuK α radiation source and recorded in the 2θ range of 20–80°.

2.4 *Photocatalysis*

The photocatalytic decomposition of methyl orange (MO) was performed with the film catalysts immersed in a 46 ml aqueous MO solution ($5\ mg\ l^{-1}$) under UV light and visible light irradiations, respectively. A sunlamp (Philips HPA 400/30S, Belgium) was employed for the UV light photocatalytic reaction, and a 400-nm cutoff filter was employed to remove ultraviolet light for the visible light reaction. Prior to photocatalytic reactions, the MO solution with film catalyst was magnetically stirred in the dark for 0.5 h to reach the adsorption equilibrium of MO. Variations in the concentration of MO under illumination were monitored by a UV–Vis absorption spectrometer. In addition, the photocatalytic decomposition experiments of Rhodamine B (RhB) solution ($5\ mg\ l^{-1}$) and MB solution ($5\ mg\ l^{-1}$) by TiO_2–510Sn NAF were also carried out with the similar procedures.

3. Results and discussion

The morphologies of films were obtained by the SEM measurement. Figure 1 shows the SEM images of TiO_2 and TiO_2–510Sn NAFs. Both the films showed the good nanorod array structures. Figure 1a and b shows the top–down morphology of pure TiO_2 NAF, and the TiO_2 nanorods show a relatively narrow diameter size in the range of 40–140 nm. Figure 1c shows the cross-section morphology of TiO_2 film, and the nanorods exhibit a vertical state as well as a very uniform length of *ca*. 2 µm. For the TiO_2–510Sn NAF, the similar top–down and cross-section morphologies to those of pure TiO_2 were observed in figure 1d–f. The diameter and length sizes of Sn^{4+}-doped TiO_2 nanorods were close to those of pure TiO_2. In conclusion, the doping of Sn^{4+} ions had almost no effect on the morphology of TiO_2 NAF.

The crystal structures of film catalysts were characterized by XRD, and the obtained spectra are illustrated as shown in figure 2. In figure 2a, it is easy to observe that all the films demonstrated the sharp diffraction peaks in the spectra, implying the good crystallinity of samples. For TiO_2 NAF, the diffraction peaks located at 26.5, 33.8, 37.8, 51.5,

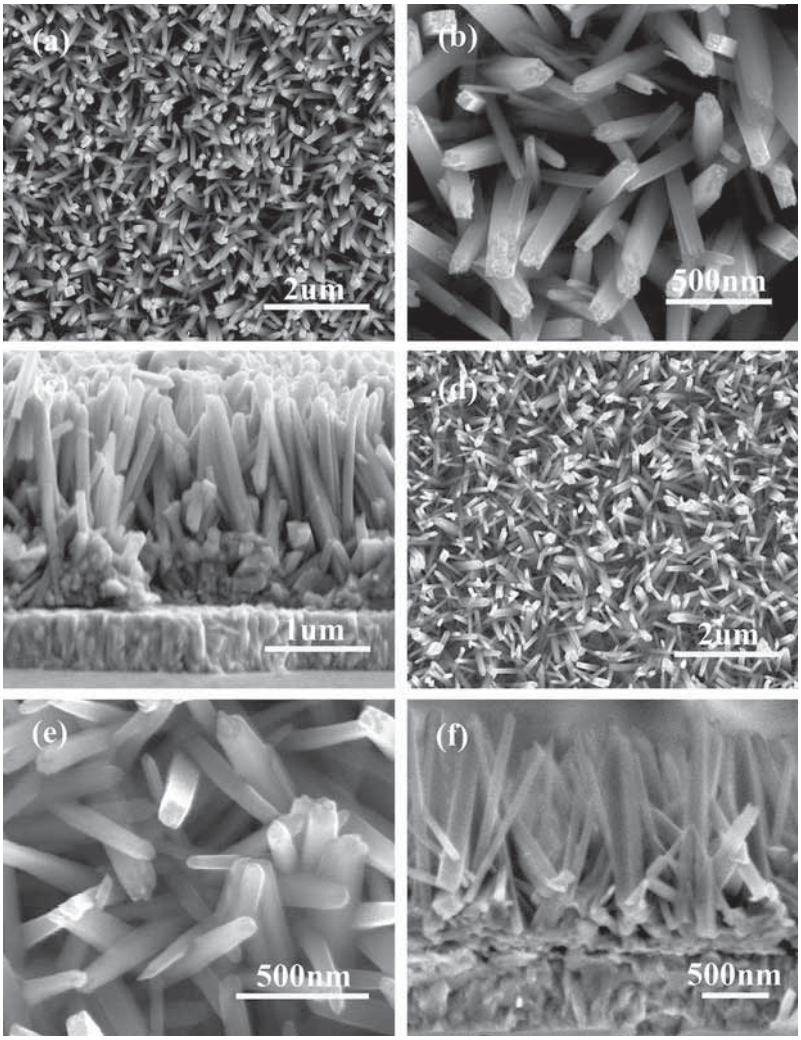

Figure 1. SEM images of TiO_2 NAF (**a**, **b**: top view; **c**: sectional view) and TiO_2–510Sn NAF (**d**, **e**: top view; **f**: sectional view).

61.6 and 65.7° were ascribed to the diffraction peaks of FTO (SnO_2, JCPDS 46-1088), and the diffraction peaks located at 27.4, 36.1, 54.4, 63.0 and 69.0° were ascribed to the rutile TiO_2 component (JCPDS 65-0192). This result suggested that the crystal phase of pure TiO_2 nanorods were rutile structures. In the patterns of Sn^{4+}-doped TiO_2 NAFs, the similar diffraction peaks were observed, which implied that the doping of Sn^{4+} did not cause the change in the rutile crystal structure of TiO_2 nanorods. Figure 2b shows the enlargement of the (101) diffraction peaks of rutile TiO_2 nanorods of pure- and doped-TiO_2 NAFs. It can be clearly seen that the position of (101) diffraction peak shifted to the lower diffraction angle gradually with the increase in the amount of Sn^{4+} dopant. Based on the corresponding doping theory, as the electronegativity and ionic radius of the Sn^{4+} ion (1.8, 69 pm) are similar to those of the Ti^{4+} ion (1.5, 53 pm) of TiO_2 [24], the doped-Sn^{4+} ions will replace lattice Ti^{4+} ions and, accordingly, occupy the positions of lattice Ti^{4+}. Because the ionic radius of Sn^{4+} ions is larger than that of Ti^{4+} ions, the doping would induce an increment in the interplanar distance. Thus, the positions of diffraction peaks for Sn^{4+}-doped TiO_2 nanorods shift to lower diffraction angles compared to pure TiO_2 nanorods as illustrated in table 1 (TiO_2: 36.14°, TiO_2–510Sn: 36.12°, TiO_2–850Sn: 36.10°). The interplanar distances of (101) for the pure and doped samples were also calculated in terms of Bragg's law [25], and the results are also summarized in table 1. It is easily found that the calculated results of interplanar distances of (101) were enlarged gradually with the increase in the doped Sn^{4+} ions (TiO_2: 2.4833 Å, TiO_2–510Sn: 2.4847 Å, TiO_2–850Sn: 2.4859 Å), which is very much in accordance with the doping theory discussed above. In addition, the quantities of Sn^{4+} ions actually doped in TiO_2 NAFs were also verified by the EDS analyses. The relative atomic percentages of Ti and Sn elements in TiO_2–340Sn, TiO_2–510Sn and TiO_2–850Sn NAFs are summarized in table 2. Obviously, the relative atomic

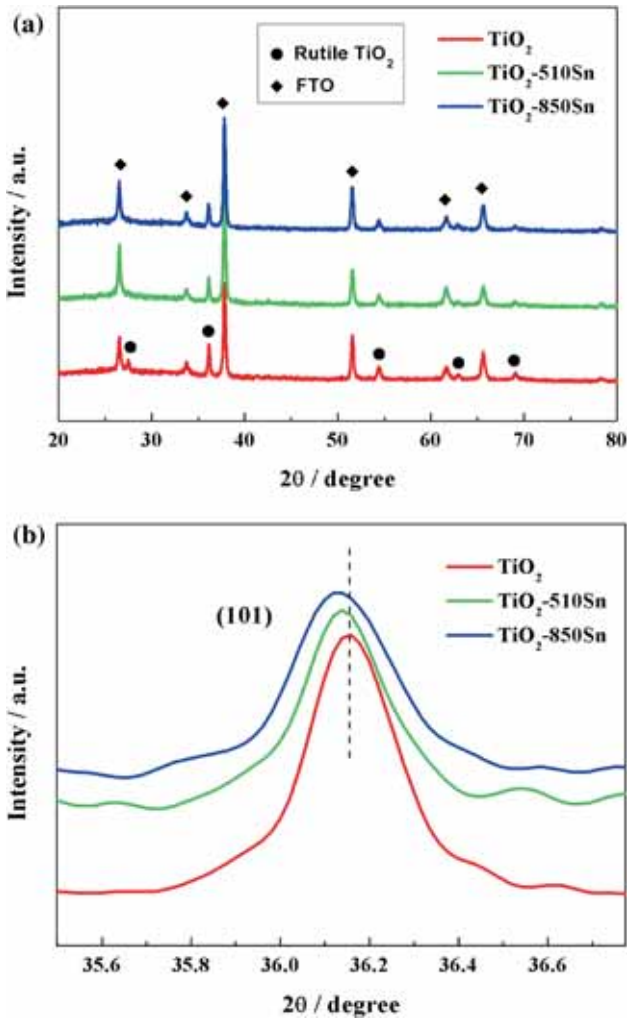

Figure 2. (**a**) XRD patterns of TiO_2, TiO_2–510Sn, TiO_2–850Sn NAFs and (**b**) the enlargement of the (101) diffraction peak of rutile TiO_2 nanorods.

Table 1. The peak positions of (101) and $d_{(101)}$ values of the TiO_2, TiO_2–510Sn and TiO_2–850Sn NAFs.

Samples	$2\theta_{(101)}$ (deg)	$d_{(101)}$ value (Å)
TiO_2	36.14	2.4833
TiO_2–510Sn	36.12	2.4847
TiO_2–850Sn	36.10	2.4859

Table 2. The relative atomic percentages of Ti and Sn elements in the TiO_2–340Sn, TiO_2–510Sn and TiO_2–850Sn NAFs determined by EDS analyses.

Samples	Ti (%)	Sn (%)	Sn/(Ti+Sn) (%)
TiO_2–340Sn	24.30	0.13	0.53
TiO_2–510Sn	28.93	0.21	0.72
TiO_2–850Sn	30.67	0.25	0.81

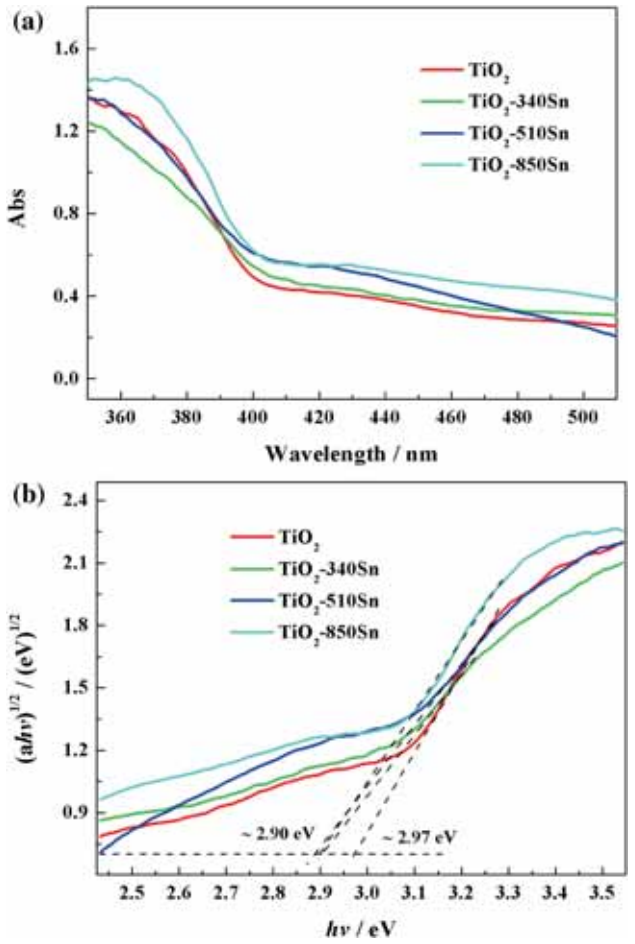

Figure 3. (**a**) DRS spectra and (**b**) Tauc plots of the TiO_2, TiO_2–340Sn, TiO_2–510Sn and TiO_2–850Sn NAFs.

percentages of Sn element for the doped NAFs increased gradually with the increase in the addition of $SnCl_4$ in the preparation process of NAFs.

Figure 3a and b shows the DRS spectra and Tauc plots of the samples of TiO_2, TiO_2–340Sn, TiO_2–510Sn and TiO_2–850Sn. In figure 3a, it can be seen that both the pure- and doped-TiO_2 NAFs had the strong absorption in the range of $\lambda > \sim 400$ nm, which corresponds to the band gap electron excitation. It is worth to note that with the increase of doping amount of Sn^{4+} ions, the doped-TiO_2 NAFs exhibited gradually enhanced visible light absorption in the range of 400–500 nm. Moreover, as shown in figure 3b, the Tauc plots showed the reduction of the band gap of doped NAFs (~2.9 eV) in comparison with that of TiO_2 NAF (~2.97 eV). Both the enhancement of visible light absorption and the reduction of band gap of doped NAFs should be attributed to the Sn^{4+} doping energy level, which are located below the conduction band of TiO_2 for ~0.4 eV [26].

The visible and UV photocatalytic activities of NAFs were evaluated by the degradation of MO solution, and the results are illustrated in figure 4 and table 3. In the case of visible-light irradiation ($\lambda > 400$ nm), TiO_2 NAF showed a degradation ratio of 12%. TiO_2–340Sn exhibited an obvious improvement of degradation ratio (22%) compared to TiO_2 NAF. With the continuous increase of doping Sn^{4+} ions, TiO_2–510Sn showed a further increase in the degradation ratio to 23.5%, which is nearly two times higher than that of pure TiO_2. However, when the doped $SnCl_4$ was increased to 850 µl, TiO_2–850Sn showed a decrease degradation ratio (15%) in contrast to TiO_2–510Sn. Therefore, with the increase of doped Sn^{4+} ions, the visible light activities of NAFs increased first and then decreased subsequently. The sample of TiO_2–510Sn demonstrated the highest activity. For the UV case, the TiO_2 NAF showed a large degradation ratio of 25%, and the doped samples of TiO_2–340Sn, TiO_2–510Sn and TiO_2–850Sn showed the degradation ratios of 26.5, 23 and 21.4%, respectively. The doping of Sn^{4+} ions did not cause the significant negative effect on the activity of film catalyst. For both the visible and UV cases, the photolysis of MO without adding catalyst were also tested as illustrated in figure 4a and b. The results demonstrated that there is nearly no apparent degradation of MO under the irradiation of visible or UV light. This implies that the degradation of MO in both the UV and visible light cases should be attributed to the photocatalytic decomposition by NAF catalysts. The plots of the photocatalytic degradation ratios of MO *vs*. percentages of Sn/(Ti+Sn) for TiO_2, TiO_2–340Sn, TiO_2–510Sn and TiO_2–850Sn NAFs under visible- and UV-light irradiations are illustrated in figure 5. Figure 6 shows the linear fitting of $\ln(C_0/C) \sim t$ curves for all the samples under visible and UV photocatalyses. It can be found that the dynamics of photocatalytic degradation of MO for all the samples were in accord with the pseudo-first-order kinetic characteristic. The fitted apparent degradation rate constants (k) are summarized in table 3. The similar change trend of rate constants with that of degradation ratios was observed. All the doped films displayed the higher rate constants than that of TiO_2 in the visible case, and TiO_2–510Sn showed the highest rate constant (more than twice that of TiO_2), implying the obvious improvement of photocatalytic ability by means of Sn^{4+} doping. In the case of UV photocatalysis, all the doped films maintained the similar values of rate constants with that of TiO_2 NAF. In addition, the photocatalytic decompositions of RhB and MB with TiO_2–510Sn were also carried out under the visible and UV light irradiations. The results, as shown in figure 7, demonstrated that the doped NAF still had a strong photocatalytic ability to decompose RhB and MB, implying the unselective photocatalytic activity of the Sn^{4+}-doped TiO_2 NAF.

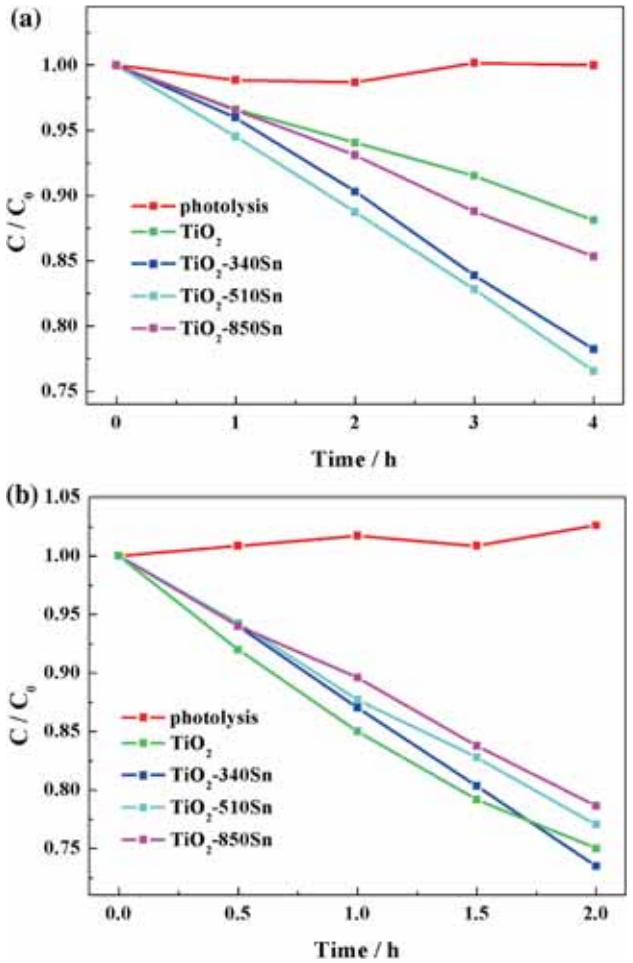

Figure 4. Photocatalytic degradation of MO on pure TiO_2, TiO_2–340Sn, TiO_2–510Sn and TiO_2–850Sn NAFs under (**a**) visible and (**b**) UV irradiations.

Table 3. The detailed results of photocatalytic degradation of MO with the TiO_2, TiO_2–340Sn, TiO_2–510Sn and TiO_2–850Sn NAFs under the visible and UV light irradiations.

	Visible		UV	
Samples	Degradation ratio (%)	Rate constant k (h^{-1})	Degradation ratio (%)	Rate constant k (h^{-1})
TiO_2	12	0.0307	25	0.1451
TiO_2–340Sn	22	0.0626	26.5	0.1546
TiO_2–510Sn	23.5	0.0667	23	0.1303
TiO_2–850Sn	15	0.0401	21.4	0.1193

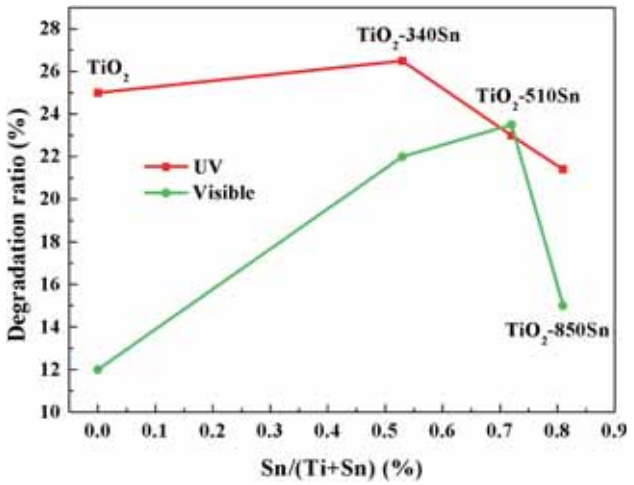

Figure 5. Plots of photocatalytic degradation ratios of MO *vs*. percentages of Sn/(Ti+Sn) for TiO_2, TiO_2–340Sn, TiO_2–510Sn and TiO_2–850Sn NAFs under visible and UV irradiations.

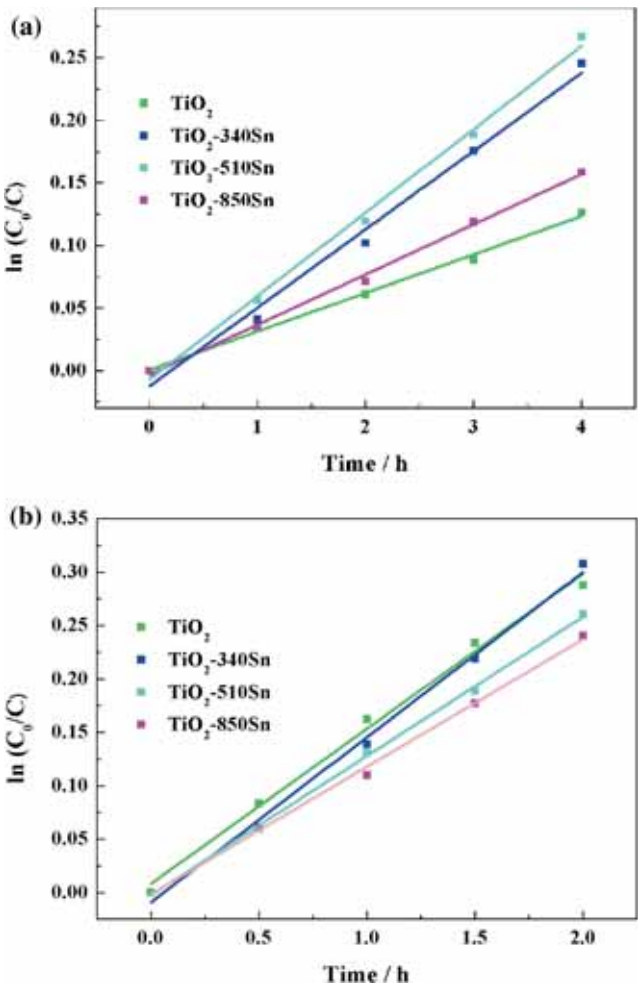

Figure 6. The pseudo-first-order kinetics curves of MO degradation as a function of irradiation time for TiO_2, TiO_2–340Sn, TiO_2–510Sn and TiO_2–850Sn NAFs under (**a**) visible and (**b**) UV irradiations.

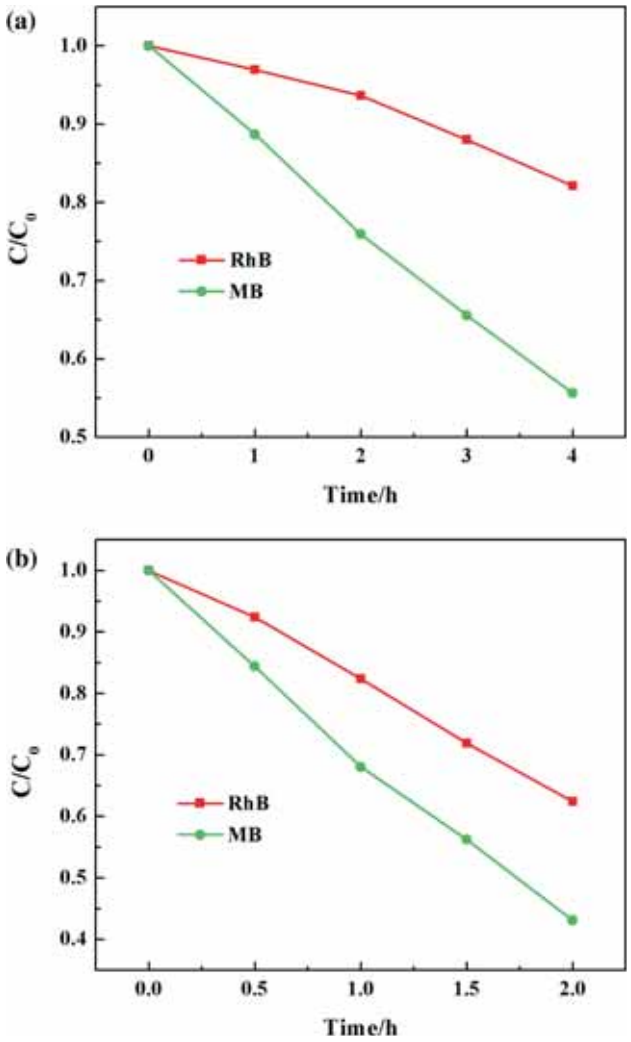

Figure 7. Photocatalytic degradation of RhB and MB on TiO_2–510Sn NAF under (**a**) visible and (**b**) UV irradiations.

For better understanding of the photocatalytic results, the band structure as well as the photocatalytic mechanism of Sn^{4+}-doped TiO_2 NAFs are illustrated in figure 8. Due to the weak absorption of visible light of rutile crystal phase owing to the band gap transition of valence band electrons (process 1) and large specific surface area of rod array structure, TiO_2 NAF exhibited a weak activity under the visible light irradiation. After the doping of Sn^{4+}, the Sn^{4+} doping energy level located below the conduction band would cause the enhanced visible light absorption of catalysts (figure 3) due to the transition of photogenerated electron from valence band to Sn^{4+} doping level (process 4) as shown in figure 8. Moreover, in virtue of the role of metal ion dopant as the direct mediator of the interfacial charge transfer [27], part of the band transition photogenerated electrons would prefer to migrate and be trapped by the Sn^{4+} doping energy level (process 3) and then, easily transferred to the catalyst surface to participate in photocatalytic reaction, which would inhibit the band recombination

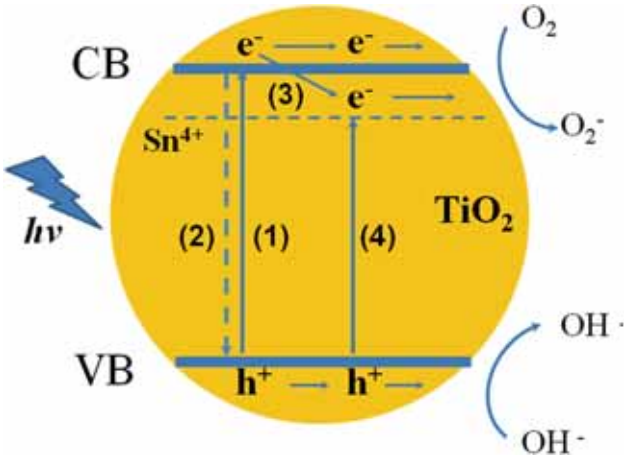

Figure 8. Schematic diagram for the band structure of Sn^{4+} ions-doped TiO_2 and the photocatalytic mechanism.

of photogenerated carriers of TiO_2 (process 2) to a certain extent [26–28]. Therefore, the synergistic effects of enhanced visible light absorption and inhibition of photogenerated carrier recombination would result in the obvious improvement of photocatalytic activity for doped NAFs. With the increase in the addition of $SnCl_4$ in the preparation process of doped NAFs, the more Sn^{4+} ions were doped in TiO_2–510Sn (table 2), which would result in the stronger visible light absorption and carriers separation, and subsequently the higher visible activity. For TiO_2–850Sn, the decrease of visible activity should be ascribed to the too much doped Sn^{4+} ions in TiO_2, which may act as the recombination centre of carriers and thus, reduce their separation efficiency [29]. The reduced distance between the doped Sn^{4+} ion trapping sites in the TiO_2 nanorod decreased with the increase of dopant, and the trapping sites would promote the recombination of photogenerated carriers instead of inhibiting effect [29]. In the UV case, because the intensity of UV light is much higher than that of visible light, the band gap excitation is the primary path for the generation of photogenerated carriers, and the pure and Sn^{4+} ions-doped TiO_2 NAFs exhibited the similar UV photocatalytic activities.

4. Conclusions

Sn^{4+}-doped and pure TiO_2 NAFs on the FTO conducting glass were successfully prepared by the facile hydrothermal method. The pure TiO_2 NAF consists of nanorods with a diameter size range of 40–140 nm and a length of *ca.* 2 μm. The Sn^{4+} ion-doping had nearly no effect on the morphology of TiO_2 NAF, but an enlargement of interplanar distance of the lattice of TiO_2 was observed, which was attributed to the entrance of Sn^{4+} ions into the unit cell of TiO_2 nanorod and subsequently, replacement to the lattice Ti^{4+} ions. Due to the doping energy level of Sn^{4+} ions below the conduction band, Sn^{4+}-doped TiO_2 NAFs showed the enhanced visible light absorption and improved photogenerated carrier separation, both of which led to the significant improvement of visible activities of the doped NAFs photocatalysts. It is hopeful that the obtained Sn^{4+}-doped TiO_2 NAFs in this study would have the excellent applications in the fields of photocatalysis, photoelectric catalysis, solar cell and the other photoelectric devices in the future.

Acknowledgements

This study was supported by the projects from National Natural Science Foundation of China (51202090, 51572109), the program for Taishan Scholars, China Postdoctoral Science Foundation (2016M602138), Shandong Province Higher Educational Science and Technology Program (J17KA002), Outstanding Young Scientists Foundation Grant of Shandong Province (BS2012CL004), Doctoral Foundation of University of Jinan, China (XBS1027), and Natural Science Foundation of University of Jinan, China (XKY1601).

References

[1] Asahi R, Morikawa T, Irie H and Ohwaki T 2014 *Chem. Rev.* **114** 9824
[2] Zhang N, Yang M, Liu S, Sun Y and Xu Y 2015 *Chem. Rev.* **115** 10307
[3] Momeni M M 2016 *Bull. Mater. Sci.* **39** 1389
[4] Cao Y, Yu Y, Zhang P, Zhang L, He T and Cao Y 2013 *Sep. Purif. Technol.* **104** 256
[5] Mahadwad O K, Parikh P A, Jasra R V and Patil C 2011 *Bull. Mater. Sci.* **34** 551
[6] Cao Y, He T, Zhao L, Wang E, Yang W and Cao Y 2009 *J. Phys. Chem. C* **113** 18121
[7] Cao Y, He T, Chen Y and Cao Y 2010 *J. Phys. Chem. C* **114** 3627
[8] Bai X, Wang L, Zong R, Lv Y, Sun Y and Zhu Y 2013 *Langmuir* **29** 3097
[9] Tomita O, Otsubo T, Higashi M, Ohtani B and Abe R 2016 *ACS Catal.* **6** 1134
[10] Wu S, Xiong J, Sun J, Hood Z, Zeng W, Yang Z *et al* 2017 *ACS Appl. Mater. Interfaces* **9** 16620
[11] Li W, Jia X, Li P, Zhang B, Zhang H, Geng W *et al* 2015 *ACS Sustain. Chem. Eng.* **3** 1101
[12] Huang Y, Li H, Balogun M, Liu W, Tong Y, Lu X *et al* 2014 *ACS Appl. Mater. Interfaces* **6** 22920
[13] Wang J, Yao H, Fan Z, Zhang L, Wang J, Zang S *et al* 2016 *ACS Appl. Mater. Interfaces* **8** 3765
[14] He Y, Zhang L, Teng B and Fan M 2015 *Environ. Sci. Technol.* **49** 649
[15] Schneider J, Matsuoka M, Takeuchi M, Zhang J, Horiuchi Y, Anpo M *et al* 2014 *Chem. Rev.* **114** 9919
[16] Shah M, Park A, Zhang K, Park J and Yoo P 2012 *ACS Appl. Mater. Interfaces* **4** 3893

[17] Nursam N, Wang X and Caruso R 2015 *ACS Comb. Sci.* **17** 548
[18] Xiao F 2012 *ACS Appl. Mater. Interfaces* **4** 7055
[19] Zhou J, Lv L, Yu J, Li H, Guo P, Sun H *et al* 2008 *J. Phys. Chem. C* **112** 5316
[20] Long L, Zhang A, Yang J, Zhang X and Yu H 2014 *ACS Appl. Mater. Interfaces* **6** 16712
[21] Han X and Shao G 2011 *J. Phys. Chem. C* **115** 8274
[22] Fu K, Huang J, Yao N, Xu X and Wei M 2015 *Ind. Eng. Chem. Res.* **54** 659
[23] Liu J, Yu X, Liu Q, Liu R, Shang X, Zhang S *et al* 2014 *Appl. Catal. B: Environ.* **158–159** 296
[24] Xu Y L 1991 *The basics of semiconducting oxides and compounds* (China: Press of Xi'an University of Electronic Science and Technology)
[25] Lin J, Yu J, Lo D and Lam S 1999 *J. Catal.* **183** 368
[26] Cao Y, Yang W, Zhang W, Liu G and Yue P 2004 *New J. Chem.* **28** 218
[27] Choi W, Termin A and Hoffmann M 1994 *J. Phys. Chem.* **98** 13669
[28] Wang E, He T, Zhao L, Chen Y and Cao Y 2011 *J. Mater. Chem.* **21** 144
[29] Cong Y, Zhang J, Chen F, Anpo M and He D 2007 *J. Phys. Chem. C* **111** 10618